Decoupling of rotational and translational diffusion in supercooled colloidal fluids

Kazem V. Edmond[a,1], Mark T. Elsesser[b], Gary L. Hunter[a,1], David J. Pine[b], and Eric R. Weeks[a,2]

[a]Physics Department, Emory University, Atlanta, GA 30322; and [b]Center for Soft Matter Research, Department of Physics, New York University, New York, NY 10003

Edited by T. C. Lubensky, University of Pennsylvania, Philadelphia, PA, and approved September 18, 2012 (received for review March 14, 2012)

We use confocal microscopy to directly observe 3D translational and rotational diffusion of tetrahedral clusters, which serve as tracers in colloidal supercooled fluids. We find that as the colloidal glass transition is approached, translational and rotational diffusion decouple from each other: Rotational diffusion remains inversely proportional to the growing viscosity whereas translational diffusion does not, decreasing by a much lesser extent. We quantify the rotational motion with two distinct methods, finding agreement between these methods, in contrast with recent simulation results. The decoupling coincides with the emergence of non-Gaussian displacement distributions for translation whereas rotational displacement distributions remain Gaussian. Ultimately, our work demonstrates that as the glass transition is approached, the sample can no longer be approximated as a continuum fluid when considering diffusion.

Rapidly cooling a glass-forming liquid fundamentally changes the nature of fluid transport at a molecular scale (1–7). For a tracer in a continuum fluid, the translational and rotational diffusion coefficients D_T and D_R, respectively, depend on temperature T and viscosity η as $D \propto T/\eta$. Therefore, the ratio D_T/D_R is a constant that is independent of both T and η. However, this relationship breaks down in the deeply supercooled regime near the glass transition, according to experiments with molecular glass formers and also molecular dynamics simulations (1–3, 8–14).

Experiments with glass-forming materials find that rotational diffusion remains strongly coupled with viscosity, where $D_R \propto \eta^{-1}$, whereas translational diffusion decouples, developing a fractional dependence on η where $D_T \propto \eta^{-\xi}$ with $\xi < 1$ (2, 8, 15). Near the glass transition, D_T can be enhanced by two orders of magnitude over what would be calculated from the material's viscosity. The rotational diffusion coefficients from these experiments are inferred from measurements related to molecular rotations, and are evaluated using the "Debye model" due to an inability to directly observe molecular rearrangements in a material's bulk (3, 8–10, 16, 17). This experimental limitation has inspired computational studies where diffusion can be calculated using the Debye model and also a complementary method, the "Einstein formulation," which is more directly related to the trajectories of the diffusing objects. These simulations studied pure systems of water (9), *ortho*-terphenyl (10), and hard dumbbell particles (11). Intriguingly, the simulations found that decoupling depends qualitatively on the analysis method: They find rotational motion is enhanced over translational motion when quantified with the Einstein formulation, with the opposite being true in the Debye formulation. The results from these simulations raise the need for a critical reexamination of our current understanding of the relationship between translational and rotational diffusion, and only through direct observation can these differences be addressed (10). Unfortunately, there has been no direct experimental observation of diffusive decoupling in a 3D system which would allow for these findings to be tested.

We use high-speed confocal microscopy to directly visualize the 3D translational and rotational motion of tetrahedral tracer colloidal clusters in a dense amorphous suspension of colloidal spheres. A glass transition occurs as the colloidal suspension's volume fraction is increased above the value of $\phi_G \sim 0.58$ (18, 19). We observe that as the glass transition is approached from $\phi < \phi_G$, the long-time rotational diffusion of the tracers decreases proportionally with the bulk viscosity η, whereas long-time translational diffusion decreases by a much lesser extent, similar to observations made with molecular glasses (2, 8). Moreover, we quantify the rotational motion in several ways, and find that all rotational observations remain proportional to η^{-1}. Our results are in contrast with the aforementioned results from computer simulations (9–11), where the details depend on the analysis method, and rotational diffusion was either apparently enhanced or suppressed depending on the analysis. Our results persist regardless of the analysis used to characterize diffusion. Direct comparison between our results and those of computer simulations is problematic, given that they studied pure liquids whereas we study tracers; these differences are evaluated in the *Discussion*.

Colloidal suspensions provide an insightful avenue for experimentally exploring the glass transition (18–22). The key control parameter is the volume fraction ϕ, rather than temperature. As ϕ increases, colloidal microspheres exhibit phase behavior that is in good agreement with the hard-sphere model (18, 19). Hard spheres are arguably the simplest system in which to study the most fundamental features of the glass transition. An important advantage of colloids is that individual particles can be followed in 3D using a confocal microscope, which permits direct observation of the complex dynamical processes of individual particles (22–25) that can be difficult to study with more conventional methods that average over many particles within the sample's bulk (2, 16).

Steric effects are key to understanding the colloidal glass transition: Particles cannot overlap one another, complicating their motion in a dense sample. For one sphere to move, its neighbors must move out of its way, and their neighbors must move out of their way, etc. This leads to large-scale rearrangements involving many particles (22, 25–27). In contrast, rotation of spheres is possible without colliding with neighboring particles. Rotation of optically anisotropic colloidal spheres has been studied (28–31). These rotations do slow near the colloidal glass transition, but due to hydrodynamic interactions rather than steric interactions. For this reason, in dense suspensions of spheres rotational diffusion is faster than translational diffusion (30); this is discussed further in *Materials and Methods*. The hydrodynamic slowing of rotational diffusion, while interesting in its own right, cannot speak to the question of slowing rotational diffusion in molecular glasses.

Therefore, we use a dispersion of isolated nonspherical particles in a suspension of spherical particles. This is a simple physical model system in which to study rotational and translational diffusion near the glass transition. Our nonspherical tracer particles, developed

Author contributions: K.V.E. and E.R.W. designed research; K.V.E. performed research; M.T.E., G.L.H., and D.J.P. contributed new reagents/analytic tools; K.V.E. and G.L.H. analyzed data; and K.V.E., D.J.P., and E.R.W. wrote the paper.

The authors declare no conflict of interest.

This article is a PNAS Direct Submission.

[1]Present address: Center for Soft Matter Research, Department of Physics, New York University, New York, NY 10003.

[2]To whom correspondence should be addressed. E-mail: weeks@physics.emory.edu.

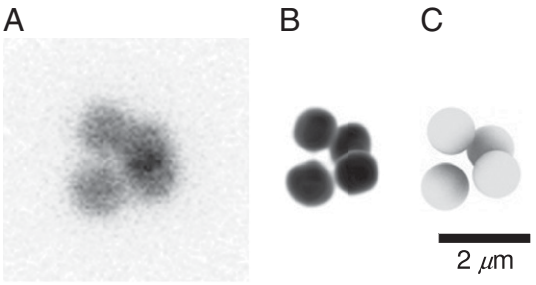

Fig. 1. Visual representations of a colloidal tetrahedral cluster. Only the core of each particle is fluorescently labeled, surrounded by a blank undyed shell of PMMA, making each particle visually distinct from its clustered neighbors. (*A*) Composite, imaged using a confocal microscope and calculated by taking the mean of a 3D image. The composite images allow us to see through the cluster, where the overlap between multiple particles appears black. (*B*) Three-dimensional reconstruction. (*C*) Three-dimensional rendering of spheres at the centers of the particle coordinates, as determined by our tracking algorithms (38, 41). Sphere diameters are roughly equal to that of the fluorescent cores.

through recent advances in colloidal science (32), are highly ordered clusters of colloidal particles (33). A confocal micrograph of one such cluster with corresponding 3D representations is shown in Fig. 1. The rotational motion of such clusters is hindered by collisions with neighboring spherical particles, and thus is a reasonable model of steric hindrances within molecular glass-forming systems. At short time scales, hydrodynamics are still expected to be important (30, 31); however, we focus on the long-time dynamics, for which the steric hindrance should be most significant (34–37).

With a recently developed means of tracking motion of such clusters (38), we are in a position to simultaneously study translational and rotational diffusion of anisotropic tracers in glassy and otherwise densely packed systems. Our system can be thought of as a 3D analog of samples used in very recent colloidal experiments, where rotational diffusion was studied in dense 2D samples of colloidal ellipsoids, with aspect ratios of ∼1.1 (39) and ∼6.0 (40). We follow the full 3D motion of our clusters, allowing us to observe rotations around any axis without any ambiguity, as discussed in *Materials and Methods*.

Results

We track the translational and rotational diffusion of the tracer particles in 3D (38, 41). A selection of respective trajectories is shown in Fig. 2. The random translational and angular Brownian motion of a particle is characterized by corresponding diffusion coefficients. For an arbitrary 3D object possessing no special symmetries, there are three translational and three rotational diffusion coefficients. Because of its high symmetry, however, the diffusive motion of a tetrahedron is characterized by only one translational and one rotational diffusion coefficient (42). Therefore, we can quantify the tracer mobility in this system using only the mean-square displacement (MSD) of the center of mass and the mean-square angular displacement (MSAD) as described below.

The MSD, plotted in Fig. 3*A*, grows in time without bound according to the relation

$$\left\langle \Delta\vec{r}^{\,2}(\Delta t)\right\rangle = \left\langle \left[\vec{r}(t+\Delta t)-\vec{r}(t)\right]^2\right\rangle \quad [1]$$

$$\lim_{\Delta t\to\infty}\left\langle \Delta\vec{r}^{\,2}(\Delta t)\right\rangle = 6D_{\mathrm{T}}\Delta t. \quad [2]$$

Here, $\vec{r}(t)$ is the position of the tracer particle center of mass at time t, and the angle brackets indicate averages over all initial times t. Thus, we obtain the translational diffusion coefficient D_{T} from a measurement of the MSD. The "Einstein formalism" for rotational motion is an analogous method of quantifying rotational motion of a unit vector $\hat{\mathbf{u}}$, which we define as an orientation vector that extends from the cluster's center to an arbitrary initial direction (9). The cross-product $\hat{\mathbf{u}}(t)\times\hat{\mathbf{u}}(t+\Delta t)$ gives the direction of the instantaneous axis of rotation for a vector rotational displacement $\Delta\vec{\varphi}(t)$, whose magnitude is given by $|\Delta\vec{\varphi}(t)| = \cos^{-1}(\hat{\mathbf{u}}(t)\cdot\hat{\mathbf{u}}(t+\Delta t))$. We can define the total angular displacement with the following integral (9):

$$\vec{\varphi}(t) = \int_0^t \Delta\vec{\varphi}(t')dt'. \quad [3]$$

The unbounded MSAD is then given by

$$\left\langle \Delta\vec{\varphi}^{\,2}(\Delta t)\right\rangle = \left\langle \left[\vec{\varphi}(t+\Delta t)-\vec{\varphi}(t)\right]^2\right\rangle \quad [4]$$

$$\lim_{\Delta t\to\infty}\left\langle \Delta\vec{\varphi}^{\,2}(\Delta t)\right\rangle = 4D_{\mathrm{R}}\Delta t, \quad [5]$$

analogous to the MSD defined in Eq. **1**. Thus, we obtain a measurement of the rotational diffusion coefficient D_{R} as well as a direct comparison between the MSAD and MSD. If the rotational trajectory is considered only about a single axis of rotation, significant motions may be overlooked. Therefore, we consider four orientation vectors $\hat{\mathbf{u}}$, each extending from the cluster's center to the center of each of the clustered particles. We evaluate the MSADs for each vector and then calculate their mean: The MSAD is the average of the four orientation vectors. We plot the MSAD in Fig. 3*B*. Note that the data for $\phi\sim 0.51$ are from a pentamer, $n = 5$ particles arranged as a triangular dipyramid (33); for these data we average over five orientation vectors. The pentamer's motion follows the same trend as seen for the tetrahedra, as quantified by the MSD and MSAD, despite its break in symmetry.

We determine D_{T} and D_{R} by finding the slope over the moderate-to-large Δt regimes of the MSD and MSAD curves; the exact procedure is described in *Materials and Methods*. We plot D_{T} and D_{R} on shared axes in Fig. 4 in terms of both ϕ and

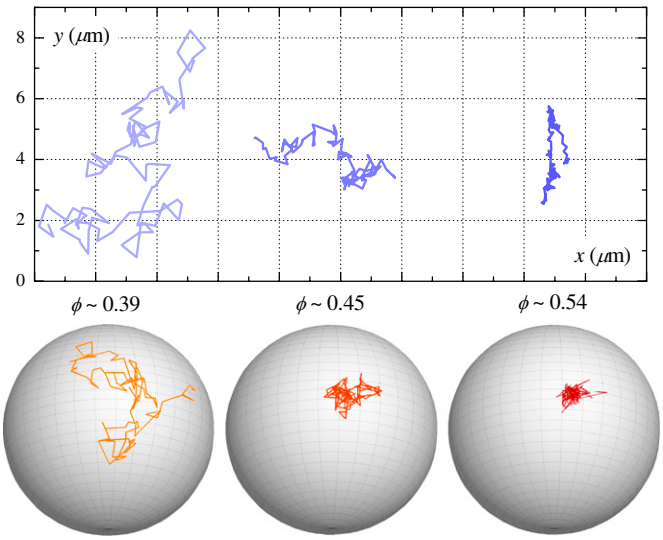

Fig. 2. Translational and rotational trajectories for clusters at different ϕ. (*Upper*) Two-dimensional projections of 3D trajectories of the center of mass of clusters. (*Lower*) Rotational trajectories depicted by a trace of a cluster's orientation across the surface of a unit sphere in the cluster's translating frame of reference. Each trajectory spans a duration of 3000 s. The translational trajectories only share the same set of axes for comparison and are each from a unique sample.

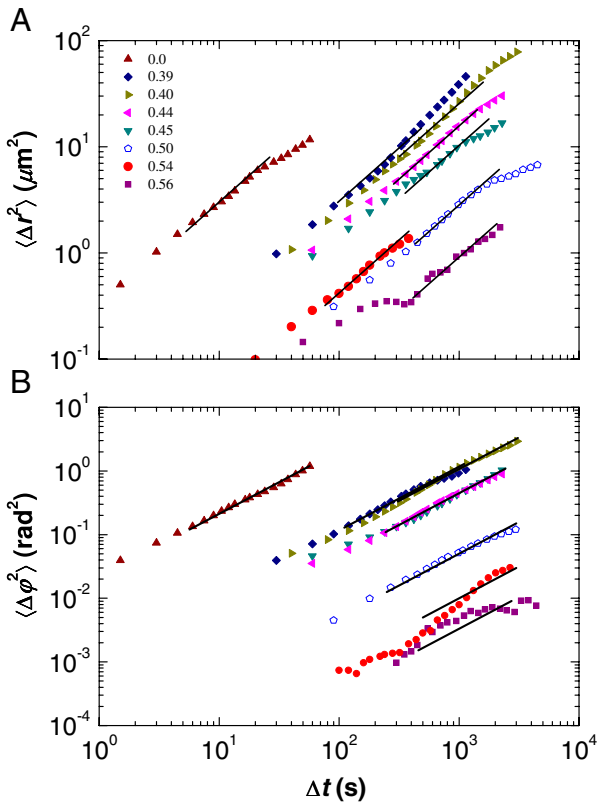

Fig. 3. Translational and rotational mobility for range of volume fractions ϕ. (*A*) MSD $\langle \Delta r^2(\Delta t)\rangle$. (*B*) MSAD $\langle \Delta\varphi^2(\Delta t)\rangle$. The open symbols are from a pentamer cluster, the closed symbols are from tetrahedra. The solid straight lines show a slope of 1 and indicate the measured value of D_T or D_R. Uncertainty due to optical noise varies between each data set: Data for $\phi \sim 0.56$ are noisier than for $\phi \sim 0.50$ and 0.54. Data below the noise floor are not plotted (38). The deviations from slope = 1 seen at large Δt values are due to lack of data; this is discussed in *Materials and Methods*.

the sample viscosity η, where η has been interpolated from data reported in ref. 43, which studies monodisperse particles. The viscosities of our bidisperse mixture could be a factor of 2 less for $\phi \sim 0.50$ (44).

As can be seen, the data in Fig. 3 do not perfectly follow the slope = 1 lines, and the resulting uncertainties in the determinations of the diffusion coefficients are reflected in the error bars in Fig. 4. Rotational diffusion remains coupled with η for the full range of ϕ, whereas translational diffusion decouples for $\phi \geq 0.51$. Numerous experiments and simulations have found that D_T in supercooled molecular glass formers scales with $\sim \eta^{-\xi}$, where $0.73 < \xi < 0.87$ depending on the specific type of material (2, 8, 45). For comparison, we include lines with slopes of −0.73 and −0.87 in Fig. 4. The decoupling is clear: the difference between D_T and D_R is well above our uncertainty level. In our densest samples, the ratio D_T/D_R is about 25 times larger than its value at $\phi \sim 0$. The diffusion coefficients for the pentamer, denoted by the open symbols in Fig. 4, are slightly lower than the trend set by data for tetrahedra, which is sensible as the pentamer will diffuse slower than the smaller tetrahedra.

Alternatively, as discussed, we can calculate the rotational diffusion using the "Debye formalism," which is analogous to what is measured from molecular glass formers using dielectric relaxation and related methods (2, 16). Again, consider the unit vector $\hat{\mathbf{u}}$ pointing from the cluster's body center to one of the particles in the cluster. One can define the reorientational time-correlation function $C_{reor}(\Delta t) = \langle \hat{\mathbf{u}}(t+\Delta t)\cdot\hat{\mathbf{u}}(t)\rangle$ (16). In a simple liquid, this decays exponentially with Δt as $C_{reor}(\Delta t) = \exp[-2D_R\Delta t]$. The values of D_R measured in this way from our data are indicated by the squares in Fig. 4, showing excellent agreement with the MSAD results. Again, we average over all four unit vectors $\hat{\mathbf{u}}$ for each tetrahedron.

We find a significant difference between the distributions of rotational and translational displacements. Rotational displacements are defined by Eq. **3** as $\Delta\vec{\varphi}(\Delta t) = |\vec{\varphi}(t+\Delta t) - \vec{\varphi}(t)|$. In all cases, the distributions of rotational displacements are Gaussian, whereas the distributions of displacements $\Delta r(\Delta t)$ show marked non-Gaussian tails for $\phi > 0.5$; see Fig. 5. That is, relatively large displacements $\Delta\vec{r}$ are rare, but not as rare as would be expected based on fitting a Gaussian to the more common smaller displacements. The largest displacements in Fig. 5*C* are on the order of 2 μm, roughly the diameter of a single particle, which is significant within a crowded environment of bidisperse particles (46). Non-Gaussian distributions are frequently seen for displacements in supercooled liquid samples (2, 12, 22, 26) and have also been seen for rotational displacements in simulation (9, 10). These distributions are typically associated with trajectories dominated by cage trapping and cage rearrangements, with the large displacements corresponding to the latter (12, 13, 22). We do not see obvious cage-rearrangement events in the trajectories (Fig. 2). It is possible that these events are obscured due to the somewhat larger size of the tracer particle compared with the bath particles (47).

The distributions of Fig. 5 raise the question of how the translational and rotational displacements relate to each other (30). In Fig. 6 *A* and *B* we show scatter plots of these two types of displacements. The horizontal and vertical dashed lines indicate the mean values of Δr and $\Delta\varphi$, so points in the upper-right quadrant correspond to large displacements of both types. For both the low volume fraction data (*A*, ϕ = 0.393) and the high volume fraction data (*B*, ϕ = 0.540), there are often times when both Δr and $\Delta\varphi$ are large. However, this seems to occur slightly more often for the higher volume fraction: there are significantly more points

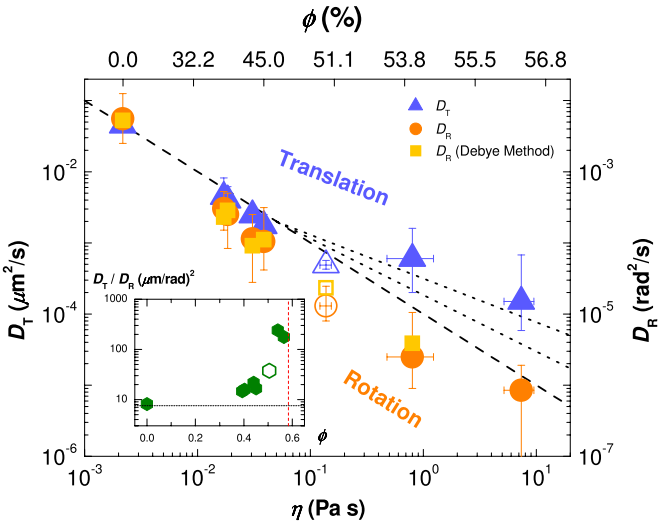

Fig. 4. Diffusion coefficients of tracer clusters for different η and ϕ. The values of η (*Lower*) are interpolated from the data published in ref. 43 using our own ϕ values (*Upper*). Both vertical axes have the same scale but have been shifted to overlap the coefficients at ϕ = 0.0. Blue triangles: translational diffusion coefficients D_T (*Left* axis). Orange circles: rotational diffusion coefficients D_R (*Right* axis). Open symbols: data from a pentamer, n = 5 particles arranged as a triangular dipyramid (33). Light orange squares: rotational diffusion coefficients calculated using the Debye formalism. Dashed and dotted lines show, from bottom up, η^{-1}, $\eta^{-0.87}$, and $\eta^{-0.73}$ dependencies. (*Inset*) Ratio between diffusion coefficients. The horizontal dashed line is the zero-concentration diffusivity ratio $\frac{D_T}{D_R} = 4/3a^2$, where a is the tetrahedral cluster's effective radius, and the vertical line is $\phi_G \sim 0.58$.

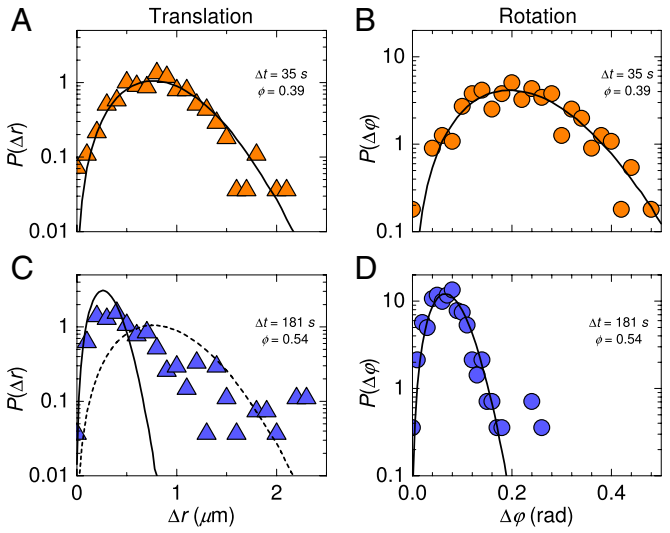

Fig. 5. Distributions for translational and rotational displacements. (*A* and *C*) Data for translational displacements (*Left*). (*B* and *D*) Data for rotational displacements (*Right*). (*Upper*) $\phi = 0.39$, with $\Delta t = 35$ s; (*Lower*) $\phi = 0.54$, with $\Delta t = 181$ s. For both, Δt is chosen so that $\langle r^2 \rangle = 1.0\ \mu m^2$. The solid lines are Gaussian fits. For comparison, we include the fit from *A* in *C* as a dashed line.

in the upper-right quadrant than in the lower-right quadrant of Fig. 6*B*. This trend is quantified in Fig. 6*C*, which shows the correlation coefficient between the two types of displacements as a function of volume fraction. The amount of correlation increases with increasing ϕ. This is counterintuitive, given that the diffusion constants D_T and D_R are decoupled. This implies that in these dense samples clusters are somewhat likely to simultaneously translate and rotate, but as $\phi \to \phi_G$ the amount of rotation decreases more strongly than the amount of translation. Fig. 6*C* also shows that for longer lag times Δt (corresponding to larger MSDs $\langle \Delta r^2 \rangle$, as given in the legend), the correlations decrease. Overall, this suggests that the tracers translate and rotate via short steps that are slightly correlated, and at long times the accumulation of these short steps is less correlated.

Discussion

One source of difference between our results and those of simulations is our use of a somewhat large rotational tracer within a fluid of smaller spherical particles, whereas simulations study pure liquids (9–11). Other molecular dynamics simulations investigated the use of tracer particles to probe sample dynamics (47, 48). These simulations varied probe size and determined that probes much larger than the bath particles modify the motion of nearby bath particles, which in turn modify the observed behavior of the probe particle (47). Likewise, experiments with molecular probes in polymer materials have found that the probe's size and shape can have a strong effect on translational diffusion (3, 14). Individual spheres within one of our clusters are close to the bath particle sizes; the cluster overall is ~2.4 times larger than the larger bath particle size. This may result in slower motion of the probe particle than the rest of the sample, given that our probes are "rough" (47, 48). Nonetheless, because the probe is not too much larger than the bath particles, it is still qualitatively linked to the bath particle dynamics. We have focused our attention on the long-time diffusive motion, which should be more coupled to the bath particle dynamics than short-time motion.

An additional point of contrast is the tracer's shape; where we use a relatively isotropic tetrahedral cluster, simulations typically use more anisotropically shaped particles such as linear dumbbells (11) or planar isosceles triangles (9, 10). It is possible that these shape differences account for the differences between our observations and the simulations; experiments have shown that tracers with different shapes can have different translational diffusion (14). Anisotropically shaped probes exhibit a characteristic change in the mechanism of reorientation, from consistently small random steps to well-separated and sudden changes of orientation (10). Large sudden angular displacements produce non-Gaussian distributions of displacement, analogous to translational cage-trapping dynamics seen in dense suspensions of colloidal microspheres (10, 22). Conversely, the decoupling in our experiments coincides with the emergence of non-Gaussian displacement distributions for translation, whereas rotational displacement distributions remain Gaussian. Our results show that the decoupling of translational and rotational diffusion occurs even with more isotropic tracer probes, as long as there are steric interactions inhibiting rotational motion.

Ultimately, the existence of decoupling between translational and rotational diffusion in our simple model system, composed of spherical "bath" particles with nonspherical tracers, demonstrates that decoupling is a generic feature of glass formers that results from crowding. As the bath particle volume fraction ϕ is increased toward the glass transition, decoupling between translational and rotational diffusion begins around $\phi \sim 0.50$, still somewhat far from the glass transition at $\phi_G \sim 0.58$. At the largest volume fraction we have studied ($\phi \sim 0.56$), the ratio of D_T/D_R is 25 times larger than it is at low volume fractions. The nature of decoupling observed here is in good agreement with measurements from molecular glass formers (2, 8). This agreement is suggestive that a wide variety of systems can exhibit decoupling. Our results clearly demonstrate that the fundamental nature of diffusion is changed near the glass transition: Whereas approximating the material as a continuum fluid is reasonable far from the glass transition, this is no longer possible close to the glass transition.

Materials and Methods

Sample Preparation. Our colloid is a suspension of spherical colloidal poly (methyl methacrylate) (PMMA) particles, sterically stabilized by a thin layer of poly(12-hydroxystearic acid) (49, 50) to prevent interparticle attraction. To prevent crystallization we use equal volume fractions of two particle species

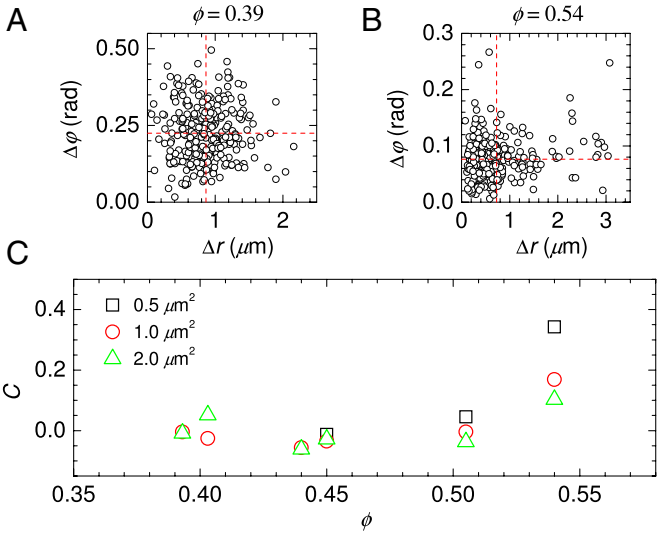

Fig. 6. Correlations between translational and rotational displacements. (*A*) Scatter plot of Δr and $\Delta\varphi$, for $\phi = 0.393$, $\langle \Delta r^2 \rangle = 1.0\ \mu m^2$, $\Delta t = 35$ s. $\Delta\varphi$ corresponds to the total rotation over each time interval. Horizontal and vertical dashed lines indicate the mean value of each type of displacement. (*B*) Similar for $\phi = 0.540$, $\langle \Delta r^2 \rangle = 1.0\ \mu m^2$, $\Delta t = 181$ s. (*C*) Correlation between Δr and $\Delta\varphi$ as a function of volume fraction, using Δt defined such that $\langle \Delta r^2 \rangle$ has the value indicated by the legend. For low ϕ, we do not take data quickly enough to see $\langle \Delta r^2 \rangle = 0.5\ \mu m^2$, so no values are plotted in such cases.

(51), 750 and 1050 nm in radius, with a polydispersity of 2.5% for each species. The particles are suspended in a mixture of ~87/13 (wt/wt) cyclohexyl bromide (CHB, Fluka, 99%) and *cis*-decahydronaphthalene (*cis*-decalin or DEC, Aldrich, 99%), which effectively matches both the density and index of refraction of the particles. To screen the repulsive charge between the particles, we saturate the solvent mixture with ~190 μM of tetrabutylammonium bromide (Aldrich, 98%) (52).

We add a trace amount of PMMA colloidal clusters, already suspended in a similar CHB/DEC mixture, synthesized using the method developed by Elsesser et al. (32). The particles in each cluster are 1300 nm in radius with 2.5% polydispersity, according to both static light-scattering measurements and calculation of diffusion coefficients using optical particle tracking techniques (32, 38, 41). Although the clustered particles stick together with van der Waals attractions, the clusters are stable and do not aggregate with other particles in even the most dense suspensions, as verified by bright-field microscopy. Only the cores of the clustered particles are fluorescently labeled (32), making the clusters easily visible among the rest of the colloid, which is invisible under fluorescent microscopy. The relatively poor z resolution of optical microscopy makes labeling only the particle cores a necessity to clearly distinguish the clustered particles from one another. Images of a core–shell cluster are shown in Fig. 1.

As described in the Introduction, we use clusters so that they sterically interact with the rest of the sample. Studies of colloidal spheres found that rotational diffusion is faster than translational diffusion (30, 31). In a colloidal suspension the spheres interact hydrodynamically, which acts to slow their rotational motion, essentially the same as how their motion is slowed near a wall (53, 54). That is, as the sample concentration is increased, spheres become closer to their neighbors, which results in slower rotational diffusion (as well as slower translational diffusion seen at short time scales, before particles have collided with one another). However, these hydrodynamic effects slow rotational diffusion by perhaps a factor of 5 (30, 55, 56), not nearly comparable to the orders of magnitude by which translational diffusion slows.

Samples are prepared by filling rectangular glass capillaries (VitroTubes, 0.10 × 2.0-mm i.d.) that are sealed with optical adhesive (Norland #68). In between the preparation of each sample, we incrementally dilute the colloid using the original supernatant, producing samples with $0.39 \leq \phi \leq 0.56$. We determine the value of ϕ for each sample by recording the mass of the colloid before and after each dilution, and then calculating the colloid's final ϕ by massing it with and without solvent (57). The values of ϕ are correct relative to each other within ±0.002 from this method and thus are reported to three significant figures in our work. However, there is an overall systematic uncertainty of ±3% from this method, which should be considered when comparing our results to those of simulations or other experiments (57).

Data Acquisition. We locate individual tetrahedral clusters within the colloid, far from other clusters and at least 35 μm from the nearest boundary to avoid wall effects. We image the clusters using a Leica TCS SP5 confocal microscope, equipped with an argon laser ($\lambda_0 = 514$ nm) and an oil-immersion objective (Leica, 63×, 1.4 N.A.). A $25 \times 25 \times 25$-μm^3 volume is scanned in 0.8 s with a pixel size of ~100 nm in x and y and 200 nm in z. The lag time Δt between each scan is adjusted from $\Delta t = 10$ to 45 s depending on the volume fraction of the sample. We set the frequency of data acquisition such that the particles displace no more than a radius between successive acquisition times, and typically far less than this. On these time scales, rotations are quite small and never more than $\pi/6$ radians (for example Fig. 5), making it clear that we do not miss any sudden large rotations that might be closer to 2π. For comparison, in a dilute sample our tetrahedral clusters translate a distance comparable to the cluster radius (2.6 μm) on a time scale of 20 s, and rotate by π radians on a time scale of 440 s (using Eqs. **1** and **4**). The result of a typical confocal scan of a diffusing cluster is shown in Fig. 1*A*. Whereas the cluster in Fig. 1 is imaged in a clear open volume of solvent, index matching of the colloid provides comparable image quality from even the most densely packed samples.

Tracking Cluster Trajectories. We identify the horizontal and vertical positions of the individual particles within a cluster to an accuracy of 0.02 and 0.04 μm, respectively, for the duration of the experiment (41). The center of mass for a cluster is found from the mean of the four individual particle positions, and so this center has an accuracy of 0.01 μm horizontally and 0.02 μm vertically. We plot the center-of-mass trajectories of tetrahedra for different ϕ in Fig. 2. To determine the cluster's orientation we follow the method described in (38). First, we define the unit vectors $\hat{\mathbf{u}}$ pointing from the cluster's body center to the center of each of the particles in the cluster. We then follow the orientation of these vectors at each successive time, thereby mapping out the rotational trajectory of the cluster. We illustrate cluster orientations in Fig. 2 as traces of the tip of one of these unit vectors on the surface of a unit sphere.

Determining Diffusion Coefficients. From the data, MSDs are calculated using Eqs. **1**, **3**, and **4**; these are shown in Fig. 3. The MSAD data for the three highest volume fractions have small displacements at short time scales, which run into issues with noise. Noise results in an additive constant independent of Δt, so for these three MSAD curves we plot $\langle \Delta\varphi^2(\Delta t)\rangle_{\text{true}} \sim \langle \Delta\varphi^2(\Delta t)\rangle_{\text{measured}} - c^2$, following the method of (57). c is estimated by inspection of the data along with the noise estimation techniques relevant for our rotational tracking method (38).

All MSD and MSAD curves in Fig. 3 are noisy as each comes from a single tracer particle. For diffusive behavior one would expect these curves to have a slope of 1 on the log–log plots of the figure. In samples near the glass transition in particular, at very short time scales ($\Delta t < 1$ s for these samples) the behavior would be diffusive, at intermediate time scales there might be a plateau in the MSD curves (slope less than 1 on a log–log plot), and at long time scales the behavior would again be diffusive, albeit with a much smaller diffusion constant (but recovering a slope of 1 on a log–log plot) (22). All our data in Fig. 3 appear to be in this long-time regime, with some hints of a plateau seen only at the shortest time scales plotted, and only for some volume fractions. In general this is because of our interest in studying the long-time dynamics, and the experimental need to avoid photobleaching of the tracers thus motivating us to take images at longer time intervals only. As noted in the Introduction, the short-time regime should be dominated by hydrodynamics and Brownian motion, whereas the long-time regime should be influenced only by steric effects and independent of the short-time dynamics (34–37). It is also possible that the plateau is below our noise level; data below our noise level are not plotted in Fig. 3.

To determine the long-time diffusion constants from these noisy MSD and MSAD curves, we (by hand) determine the best diffusion coefficient consistent with each curve. In practice, the best data come from intermediate Δt's as the long-time behavior of the MSDs has poor statistics (57). (A trajectory 5,000 s long has 10 independent instances of $\Delta t = 500$ s and only one instance of $\Delta t = 5000$ s. The noise seen at long Δt in Fig. 3 is consistent with simulations of a single Brownian tracer with a similar finite duration trajectory.) These diffusion constant fits are indicated by straight lines in Fig. 3, and the uncertainty due to the noisy MSD curves is reflected in the error bars on the diffusion constants shown in Fig. 4.

ACKNOWLEDGMENTS. K.V.E., G.L.H., and E.R.W. acknowledge support from National Science Foundation (NSF) Grant CHE-0910707. M.T.E. and D.J.P. acknowledge support from NSF Grant DMR-0706453. K.V.E. and D.J.P. acknowledge additional support from NSF Grant DMR-1105455.

1. Berthier L, Biroli G (2011) Theoretical perspective on the glass transition and amorphous materials. *Rev Mod Phys* 83(2):587–645.
2. Ediger MD (2000) Spatially heterogeneous dynamics in supercooled liquids. *Annu Rev Phys Chem* 51:99–128.
3. Cicerone MT, Ediger MD (1996) Enhanced translation of probe molecules in supercooled o-terphenyl: Signature of spatially heterogeneous dynamics? *J Chem Phys* 104 (18):7210–7218.
4. Chang I, Sillescu H (1997) Heterogeneity at the glass transition: Translational and rotational self-diffusion. *J Phys Chem B* 101(43):8794–8801.
5. Angell CA (1995) Formation of glasses from liquids and biopolymers. *Science* 267 (5206):1924–1935.
6. Stillinger FH (1995) A topographic view of supercooled liquids and glass formation. *Science* 267(5206):1935–1939.
7. Ediger MD (1998) Can density or entropy fluctuations explain enhanced translational diffusion in glass-forming liquids? *J Non-Cryst Solids* 235–237:10–18.
8. Swallen SF, Ediger MD (2011) Self-diffusion of the amorphous pharmaceutical indomethacin near T_g. *Soft Matter* 7(21):10339–10344.
9. Mazza MG, Giovambattista N, Stanley HE, Starr FW (2007) Connection of translational and rotational dynamical heterogeneities with the breakdown of the Stokes-Einstein and Stokes-Einstein-Debye relations in water. *Phys Rev E Stat Nonlin Soft Matter Phys* 76(3 Pt 1):031203.
10. Lombardo TG, Debenedetti PG, Stillinger FH (2006) Computational probes of molecular motion in the Lewis-Wahnstrom model for ortho-terphenyl. *J Chem Phys* 125(17):174507.
11. Chong SH, Kob W (2009) Coupling and decoupling between translational and rotational dynamics in a supercooled molecular liquid. *Phys Rev Lett* 102(2):025702.
12. Kumar SK, Szamel G, Douglas JF (2006) Nature of the breakdown in the Stokes-Einstein relationship in a hard sphere fluid. *J Chem Phys* 124(21):214501.
13. Saltzman EJ, Schweizer KS (2008) Large-amplitude jumps and non-Gaussian dynamics in highly concentrated hard sphere fluids. *Phys Rev E Stat Nonlin Soft Matter Phys* 77 (5 Pt 1):051504.

14. Hall DB, Deppe DD, Hamilton KE, Dhinojwala A, Torkelson JM (1998) Probe translational and rotational diffusion in polymers near T_g: Roles of probe size, shape, and secondary bonding in deviations from Debye-Stokes-Einstein scaling. *J Non-Cryst Solids* 235–237:48–56.
15. Zondervan R, Kulzer F, Berkhout GCG, Orrit M (2007) Local viscosity of supercooled glycerol near T_g probed by rotational diffusion of ensembles and single dye molecules. *Proc Natl Acad Sci USA* 104(31):12628–12633.
16. Williams G (1978) Time-correlation functions and molecular motion. *Chem Soc Rev* 7 (1):89–131.
17. Kulzer F, Xia T, Orrit M (2010) Single molecules as optical nanoprobes for soft and complex matter. *Angew Chem Int Ed Engl* 49(5):854–866.
18. Pusey PN, van Megen W (1986) Phase behaviour of concentrated suspensions of nearly hard colloidal spheres. *Nature* 320(6060):340–342.
19. van Megen W, Martinez VA, Bryant G (2009) Arrest of flow and emergence of activated processes at the glass transition of a suspension of particles with hard spherelike interactions. *Phys Rev Lett* 102(16):168301.
20. Underwood SM, Underwood SM; van Megen W (1993) Dynamic-light-scattering study of glasses of hard colloidal spheres. *Phys Rev E Stat Phys Plasmas Fluids Relat Interdiscip Topics* 47(1):248–261.
21. van Blaaderen A, Wiltzius P (1995) Real-space structure of colloidal hard-sphere glasses. *Science* 270(5239):1177–1179.
22. Weeks ER, Crocker JC, Levitt AC, Schofield AB, Weitz DA (2000) Three-dimensional direct imaging of structural relaxation near the colloidal glass transition. *Science* 287 (5453):627–631.
23. Dinsmore AD, Weeks ER, Prasad V, Levitt AC, Weitz DA (2001) Three-dimensional confocal microscopy of colloids. *Appl Opt* 40(24):4152–4159.
24. Prasad V, Semwogerere D, Weeks ER (2007) Confocal microscopy of colloids. *J Phys Condens Matter* 19(11):113102.
25. Kegel WK, van Blaaderen A (2000) Direct observation of dynamical heterogeneities in colloidal hard-sphere suspensions. *Science* 287(5451):290–293.
26. Kob W, Donati C, Plimpton SJ, Poole PH, Glotzer SC (1997) Dynamical heterogeneities in a supercooled Lennard-Jones liquid. *Phys Rev Lett* 79(15):2827–2830.
27. Doliwa B, Heuer A (2000) Cooperativity and spatial correlations near the glass transition: Computer simulation results for hard spheres and disks. *Phys Rev E Stat Phys Plasmas Fluids Relat Interdiscip Topics* 61(6 Pt B):6898–6908.
28. Anthony SM, Hong L, Kim M, Granick S (2006) Single-particle colloid tracking in four dimensions. *Langmuir* 22(24):9812–9815.
29. Degiorgio V, Piazza R, Bellini T (1994) Static and dynamic light scattering study of fluorinated polymer colloids with a crystalline internal structure. *Adv. Coll. Int. Sci* 48: 61–91.
30. Kim M, Anthony SM, Bae SC, Granick S (2011) Colloidal rotation near the colloidal glass transition. *J Chem Phys* 135(5):054905.
31. Degiorgio V, Piazza R, Jones RB (1995) Rotational diffusion in concentrated colloidal dispersions of hard spheres. *Phys Rev E Stat Phys Plasmas Fluids Relat Interdiscip Topics* 52(3):2707–2717.
32. Elsesser MT, Hollingsworth AD, Edmond KV, Pine DJ (2011) Large core-shell poly (methyl methacrylate) colloidal clusters: Synthesis, characterization, and tracking. *Langmuir* 27(3):917–927.
33. Manoharan VN, Elsesser MT, Pine DJ (2003) Dense packing and symmetry in small clusters of microspheres. *Science* 301(5632):483–487.
34. Tokuyama M, Yamazaki H, Terada Y (2003) Test of mean-field equations for two types of hard-sphere systems by a Brownian-dynamics simulation and a molecular-dynamics simulation. *Phys Rev E Stat Nonlin Soft Matter Phys* 67(6 Pt 1):062403.
35. Berthier L, et al. (2007) Spontaneous and induced dynamic fluctuations in glass formers. I. General results and dependence on ensemble and dynamics. *J Chem Phys* 126 (18):184503.
36. Gleim T, Kob W, Binder K (1998) How does the relaxation of a supercooled liquid depend on its microscopic dynamics? *Phys Rev Lett* 81:4404–4407.
37. Szamel G, Flenner E (2004) Independence of the relaxation of a supercooled fluid from its microscopic dynamics: Need for yet another extension of the mode-coupling theory. *Europhys Lett* 67:779–785.
38. Hunter GL, Edmond KV, Elsesser MT, Weeks ER (2011) Tracking rotational diffusion of colloidal clusters. *Opt Express* 19(18):17189–17202.
39. Yunker PJ, et al. (2011) Rotational and translational phonon modes in glasses composed of ellipsoidal particles. *Phys Rev E Stat Nonlin Soft Matter Phys* 83(1 Pt 1): 011403.
40. Zheng Z, Wang F, Han Y (2011) Glass transitions in quasi-two-dimensional suspensions of colloidal ellipsoids. *Phys Rev Lett* 107(6):065702.
41. Crocker JC, Grier DG (1996) Methods of digital video microscopy for colloidal studies. *J Colloid Interface Sci* 179(1):298–310.
42. Hoffmann M, Wagner CS, Harnau L, Wittemann A (2009) 3D Brownian diffusion of submicron-sized particle clusters. *ACS Nano* 3(10):3326–3334.
43. Cheng Z, Zhu J, Chaikin PM, Phan SE, Russel WB (2002) Nature of the divergence in low shear viscosity of colloidal hard-sphere dispersions. *Phys Rev E Stat Nonlin Soft Matter Phys* 65(4 Pt 1):041405.
44. Zaman AA, Moudgil BM (1998) Rheology of bidisperse aqueous silica suspensions: A new scaling method for the bidisperse viscosity. *J Rheol* 42(1):21–39.
45. Jung Y, Garrahan JP, Chandler D (2004) Excitation lines and the breakdown of Stokes-Einstein relations in supercooled liquids. *Phys Rev E Stat Nonlin Soft Matter Phys* 69(6 Pt 1):061205.
46. Narumi T, Franklin SV, Desmond KW, Tokuyama M, Weeks ER (2011) Spatial and temporal dynamical heterogeneities approaching the binary colloidal glass transition. *Soft Matter* 7(4):1472–1482.
47. Mackowiak SA, Noble JM, Kaufman LJ (2011) Manifestations of probe presence on probe dynamics in supercooled liquids. *J Chem Phys* 135(21):214503.
48. Zangi R, Mackowiak SA, Kaufman LJ (2007) Probe particles alter dynamic heterogeneities in simple supercooled systems. *J Chem Phys* 126(10):104501.
49. Antl L, et al. (1986) The preparation of poly(methyl methacrylate) latices in non-aqueous media. *Colloids Surf* 17(1):67–78.
50. Elsesser MT, Hollingsworth AD (2010) Revisiting the synthesis of a well-known comb-graft copolymer stabilizer and its application to the dispersion polymerization of poly (methyl methacrylate) in organic media. *Langmuir* 26(23):17989–17996.
51. Henderson SI, van Megen W (1998) Metastability and crystallization in suspensions of mixtures of hard spheres. *Phys Rev Lett* 80(4):877–880.
52. Yethiraj A, van Blaaderen A (2003) A colloidal model system with an interaction tunable from hard sphere to soft and dipolar. *Nature* 421(6922):513–517.
53. Faxén H (1922) Der widerstand gegen die bewegung einer starren kugel in einer zahen flüssigkeit, die zwischen zwei parallelen ebenen wänden eingeschlo ssen ist. *Ann Phys* 373(10):89–119. German.
54. Svoboda K, Block SM (1994) Biological applications of optical forces. *Annu Rev Biophys Biomol Struct* 23:247–285.
55. Goldman AJ, Cox RG, Brenner H (1967) Slow viscous motion of a sphere parallel to a plane wall - I Motion through a quiescent fluid. *Chem Eng Sci* 22(4):637–651.
56. Jones RB (2005) Rotational diffusion of colloidal particles near confining walls. *J Chem Phys* 123(16):164705.
57. Poon WCK, Weeks ER, Royall CP (2012) On measuring colloidal volume fractions. *Soft Matter* 8(1):21–30.